Performance Analysis of Grid Topologies and RANS Turbulence Models in Predicting Aerodynamic Drag Coefficient at Zero-yaw for an Artillery Projectile

A. Ferfouri[1], D. D. Jerković[1†], N. Hristov[1], A. V. Kari[2] and T. Allouche[1]

[1] University of Defence – Military Academy, Belgrade, 11042, Serbia
[2] Military Technical Institute, Belgrade, 11030, Serbia

†*Corresponding Author Email: damir.jerkovic@va.mod.gov.rs*

ABSTRACT

The present paper evaluates the performance of grid topologies and RANS turbulence models in predicting the aerodynamic drag coefficient of a 155mm artillery projectile by conducting steady-state computational research. The research is performed for Mach numbers from 0.5 to 3.0, assuming axisymmetric flow. Four distinct combinations of grid topology and turbulence model are investigated, where the O- and C-grid topologies are each paired with both the realizable $k-\varepsilon$ and the SST $k-\omega$ models. Compared to the experimental data across the Mach number range, the combination of O-grid with $k-\varepsilon$ model showed the smallest mean deviation of 1.64%, while the combination of O-grid with $k-\omega$ exhibited the largest mean deviation of 5.54%. In terms of drag component results, both turbulence models and grid topologies performed equally in predicting pressure and friction drag, with differences less than 6% in all Mach number cases. However, significant discrepancies were obtained in base drag prediction, especially between the two turbulence models, with differences reaching around 60% in the transonic regime. This was identified as the main contributor to the discrepancies in aerodynamic drag coefficient results among the four combinations. Furthermore, the findings indicate that the turbulence model selection impacts the zero-yaw drag prediction more than the grid topology, especially in the transonic and low supersonic cases.

1. INTRODUCTION

The primary goal of external ballistics is to describe the free flight of projectiles using accurate aerodynamic and atmospheric models. Aerodynamic drag is considered the main component of the total aerodynamic load and greatly affects the projectile range by its action, which is opposite to the velocity vector direction. This force opposing the projectile motion is the sum of three components: (1) pressure drag, (2) skin friction or viscous drag, and (3) base drag (Regodić et al., 2013). Each of these components influences the projectile's aerodynamic performance, necessitating a comprehensive analysis to ensure accurate predictions, particularly during the preliminary design stage.

Modern aerodynamics studies commonly use three primary research approaches. These are the computational fluid dynamics (CFD), analytical or semi-empirical theory, and experimental approaches. Every strategy offers benefits as well as drawbacks. The most effective way to solve a certain problem is typically to rationally integrate theoretical and experimental/CFD research (Roy, 2012).

Reynolds Averaged Navier Stokes (RANS) equations are commonly used in Computational Fluid Dynamics (CFD) analyses of many flow problems, including aerodynamic load prediction of projectiles, due to their cost-effectiveness and adequate accuracy. However, additional unknown variables related to turbulence are part of these equations. Therefore, several turbulence models have been proposed to estimate these variables quantitatively. Despite this, there is no model that is unanimously recognized as the most accurate in all areas of fluid flow research. The RANS turbulence models developed over the past decades also aim to balance solution accuracy with computational costs. The SST $k-\omega$ and realizable $k-\varepsilon$ models are the most used in analyzing flow turbulence in projectile aerodynamic studies.

NOMENCLATURE				
D	aerodynamic drag	S	reference cross-section
C_D	aerodynamic drag coefficient	q_∞	free-stream dynamic pressure
C_{D0}	zero-yaw drag coefficient	k	turbulent kinetic energy
$C_{D\sigma}^2$	yaw drag coefficient	ε	turbulent dissipation rate
C_{Dp}	pressure drag coefficient	ω	specific turbulent dissipation rate
C_{Df}	friction drag coefficient	P_{dif}	percent difference
C_{Db}	base drag coefficient	P_{div}	percent deviation
C_P	pressure coefficient	ABBREVIATION	
C_f	skin friction coefficient	CFD	Computational Fluid Dynamics
σ	total yaw or angle of attack	FVM	Finite Volume Method
M_a	Mach number	RANS	Reynolds Averaged Navier Stokes
d	projectile reference diameter	SST	Shear Stress Transport
ρ	air density	CG	Center of Gravity
V_∞	free-stream velocity	LES	Large-Eddy Simulation
p	static pressure on projectile surface	DES	Detached Eddy Simulation
p_∞	freestream static pressure	ICAO	International Civil Aviation Organization Standard
T	temperature	CFL	Courant-Friedriech-Lewy
R	air specific constant	Roe-FDS	Roe Flux-Difference Splitting Scheme
a	speed of sound	EAS	EquiAngle Skewness
κ	specific heat ratio	OQ	Orthogonal Quality
τ_w	local wall shear stress	SBLI	Shock Wave/Boundary Layer Interaction

The following references from published literature provide instances of research employing these two models, indicating their wide application and their effectiveness in predicting the aerodynamic coefficients of different projectiles. For the realizable $k-\varepsilon$ model, notable studies include those conducted by Silton (2005, 2011), DeSpirito (2008), Ma et al. (2016, 2021), Aziz et al. (2022), and Chang & Li, (2023). Similarly, the SST $k-\omega$ model have been extensively applied in the works of Jiajan et al. (2015b), DeSpirito (2017), Nicolás-Pérez et al. (2017), Decrocq et al. (2018), Ko et al. (2020), Wang & Zhuo (2021), and Paul et al. (2023).

Partial differential equations can be solved numerically by the generation of numerical grids, which has become an indispensable tool in several research fields. The numerical discretization of the computational domain in flow calculations around projectiles can be done with structured, unstructured, or hybrid grids. In both cases of two-dimensional (2D) and three-dimensional (3D) computations, O- and C-grid topologies are commonly used. The C-grid topology envelopes the projectile in C-shaped loops beginning and ending in the far wake (Jiajan et al., 2013, 2015a; Nicolás-Pérez et al., 2017; Wang & Zhuo, 2021). The O-grid topology has oval-like loops that completely encircle the projectile (Onn et al., 2001; Ibrahim & Filippone, 2007a, b; Dali & Jaramaz, 2019; Elawwad et al., 2020; Ferfouri et al., 2023).

Lutton (1989) compared the capabilities of these grid topologies in predicting the flow around a NACA 0012 airfoil and found that the numerical results of both grid topologies are satisfactory. The study exhibited that the O-grid outperforms the C-grid for certain critical flow conditions involving high Mach number, high Reynolds number, or angle of attack. However, the C-grid has several advantages over the O-grid. One of its advantages is its ease of construction. It is generally easier to construct

a C-grid to a given set of specifications than an O-grid. It is also difficult for the O-grid to concentrate the grid points in the wake region while maintaining a reasonable stretch ratio.

Numerous steady-state CFD studies have contributed to our understanding of projectile aerodynamics using various grid topologies and turbulence models. Silton (2011) performed a 3D computational study to determine the aerodynamic characteristics of the 0.50 cal. projectile. The results showed that the realizable $k-\varepsilon$ turbulence model can be used to accurately estimate zero-yaw drag in steady-state methods. Nicolás-Pérez et al. (2017) investigated several turbulence models, including DES and LES, in predicting the drag reduction of a base-bleed (BB) projectile using a 2D C-structured grid topology. It was found that the drag coefficient for a BB-off case can be reasonably predicted by steady-state RANS-based models. Aziz et al. (2022) evaluated how various base bleed exit geometries affect projectile drag. The realizable $k-\varepsilon$ model was selected for RANS equation closure with C-structured grid topology. The drag coefficient deviation between the computational and experimental values did not exceed 2.75% for the projectile with a central circular orifice. Chang and Li (2023) employed a steady-state CFD approach with the realizable $k-\varepsilon$ model to investigate the aerodynamic behavior of a 35 mm projectile. The zero-yaw drag coefficient results deviated from the experimental wind tunnel data by only 6%. DeSpirito (2017) used steady-state and transient CFD simulations to investigate the aerodynamics of a 155 mm spin-stabilized projectile at different angle-of-attack (AOA) configurations. The steady RANS simulations adequately predicted the drag force when using the SST $k-\omega$ turbulence model. Ko et al. (2020) investigated the steady-state flow around a 120 mm spinning projectile using the SST $k-\omega$ model. It was found that the predicted zero-yaw drag coefficient agrees well with reference values for Mach numbers below 1.0 but deviates for higher numbers.

Jiajan et al. (2015b) studied the aerodynamic performance of a standard 155 mm M549 projectile and an optimized design using computational methods and wind tunnel tests. The SST k–ω model and a C-structured grid topology were used. Compared to measurements, the CFD simulations revealed 6% and 3% deviations in zero-yaw drag for the standard and optimized projectiles, respectively. Elawwad et al. (2020) analyzed airflow around projectiles with conical and non-axisymmetric boattails using steady state RANS simulations and an O-structured grid topology, finding good agreement between computed and experimental drag coefficients.

These studies can be considered as a basis to understand the effectiveness of different grid topologies and turbulence models when used in estimating the aerodynamic load of projectiles. It has been revealed in previous works (DeSpirito & Heavey, 2004; Silton, 2011; Abou-Elela et. al., 2013; Nicolás-Pérez et al., 2017) that the selection of grid topology and turbulence model affects the predictions of projectile aerodynamic performance, including aerodynamic drag. However, the analysis of the discrepancies between various cases has not been sufficiently performed, particularly in terms of drag components. Accurately predicting these components is essential for research aimed at reducing drag by various techniques, whether active or passive, such as base bleed (Dali & Jaramaz, 2019; Wang & Zhuo, 2021; Aziz et al., 2022), boattail (DeSpirito, 2008; Elawwad et al., 2020), slot cavities (Ibrahim & Filippone, 2007a), or porous surface (Onn et al., 2001; Ibrahim & Filippone, 2007b). Addressing this gap in the present research enables to study the combined effect of grid topologies and turbulence models on the prediction of aerodynamic drag and its components. Additionally, this offers perspectives on the selection of grid topology and turbulence model for accurate aerodynamic predictions in projectile design.

Similar approaches have been employed in other research fields, such as hydrodynamic flow (Mulvany et al., 2004), breaking wave forces on marine structures (Qu et.al, 2021), aerodynamic characteristics of high-speed trains in crosswind (Li et. al, 2019), flow around a fighter aircraft (Guilmineau et. al, 2020), and airflow around a generic vehicle model (Ahmed model) (Wu et. al, 2014; Thomas & Agarwal, 2019). However, these studies have mostly focused on evaluating RANS models in general rather than grid topologies. The authors of these studies revealed that the SST k-ω and realizable k-ε models outperform other RANS models in predicting external flow field characteristics.

The current research builds on previous findings to assess the performance of O-grid and C-grid topologies in 2D computational prediction of the aerodynamic drag coefficient, and its components for the 155 mm M107 artillery projectile under axisymmetric flow (zero yaw). Additionally, the research evaluates the steady-state capabilities of the SST k-ω and realizable k-ε models across a range of Mach numbers, covering the three flow regimes.

This study is organized into five parts: the projectile aerodynamic model is discussed in the second part, followed by the computational approach, turbulence models, and grid generation in the third part. The comparison, analysis and discussion of the computational results are presented in the fourth part. The main conclusions are finally presented in the fifth part.

2. PROJECTILE AERODYNAMIC MODEL

The aerodynamic drag is an important factor affecting the projectile trajectory and range when traveling through a fluid medium such as air. This force, which opposes the direction of the projectile velocity vector (Carlucci & Jacobson, 2008), as illustrated in Fig. 1, affects the projectile stability and precision during flight. It is essential in external ballistics to accurately predict aerodynamic drag in order to ensure faithful modeling of projectile behavior in different scenarios. Eq. (1) represents the aerodynamic drag D experienced by the projectile at its center of pressure.

$$D = q_{\infty} \cdot S \cdot C_D \qquad (1)$$

Where are: D aerodynamic drag, C_D aerodynamic drag coefficient, $q_{\infty}=\rho V^2/2$ free-stream dynamic pressure, V_{∞} free-stream velocity, $S=\pi d^2/4$ reference cross-section, d projectile reference diameter, ρ air density.

The drag coefficient is defined as a function of the angle of attack by Eq. (2) (McCoy, 1998; Carlucci & Jacobson, 2008):

$$C_D = C_{D_0}(M_a) + C_{D_{\sigma^2}}(M_a) \cdot \sigma^2 \qquad (2)$$

Where C_D represents the coefficient of aerodynamic drag, σ total angle of attack, C_{D0} the zero-yaw drag coefficient, M_a Mach number, and $C_{D\sigma2}$ the yaw drag coefficient.

The drag coefficient can be simplified to $C_D = C_{D0}(M_a)$, assuming that the flow around the projectile is axisymmetric. In this particular case, the projectile shape and the Mach number M_a have the most significant effects on C_D. The velocity vector coincides with the projectile longitudinal axis of symmetry in an axisymmetric flow (at zero yaw, $\sigma=0$). Under these conditions, pressure drag, friction drag, and vortex drag (base drag) are the three components that form the drag coefficient (Onn et al., 2001; Regodić et al., 2013; Jiajan et al., 2015a), as presented in Eq. (3):

$$C_{D_0} = C_{D_p} + C_{D_f} + C_{D_b} \qquad (3)$$

The pressure drag coefficient C_{Dp} is the first term that arises due to the impact of normal pressure on the projectile
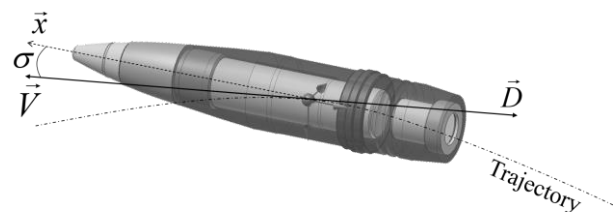

Fig. 1 Projectile aerodynamic drag

surface. It is more significant in the transonic and supersonic regimes, where shock waves are predominant. It is made up of three parts: pressure drag resulting from the projectile head (nose) C_{D1}, pressure drag resulting from the boattail C_{D3}, and pressure drag resulting from the driving band C_{D4}.

The friction drag C_{Df} is the second term, caused by air friction (viscosity) acting on the projectile surface. The third term refers to the base drag C_{Db}, which results from low pressure behind the projectile base. This coefficient mostly depends on the Mach number.

The two coefficients of pressure C_P and skin friction C_f are used for the analysis and examination of the pressure distribution and viscous effects of fluid flow along the projectile surface. These coefficients are stated as follows:

$$C_P = \frac{(p - p_\infty)}{q_\infty} \tag{4}$$

$$C_f = \frac{\tau_w}{q_\infty} \tag{5}$$

Where q_∞ denotes the free-stream dynamic pressure, p the static pressure on the projectile surface, p_∞ the freestream static pressure, and τ_w the local wall shear stress.

3. COMPUTATIONAL APPROACH

Complex interactions at high-Reynolds numbers between air and the projectile surface characterize the airflow field around a spin-stabilized projectile. This is largely influenced by projectile geometry, velocity, and surrounding atmospheric conditions. In order to accurately capture these interactions, robust methodologies are required in CFD studies to simulate boundary layers and wake regions.

3.1 Governing Equations and Turbulence Models

The conservation equations used to model compressible fluid flow (Belaidouni et al., 2016; Nicolás-Pérez et al., 2017; Dali & Jaramaz, 2019; Qiu et al., 2024) are as follows:

− RANS-based continuity equation

$$\frac{\partial \rho}{\partial t} + \frac{\partial (\rho u_i)}{\partial x_i} = 0 \tag{6}$$

− RANS-based momentum equation

$$\frac{\partial (\rho u_i)}{\partial t} + \frac{\partial (\rho u_i u_j)}{\partial x_j} = -\frac{\partial P}{\partial x_i} +$$
$$\frac{\partial}{\partial x_j}\left[\mu\left(\frac{\partial u_i}{\partial x_j} + \frac{\partial u_j}{\partial x_i} - \frac{2}{3}\delta_{ij}\frac{\partial u_l}{\partial x_l}\right)\right] + \frac{\partial}{\partial x_j}\left(-\rho\overline{u_i'u_j'}\right) \tag{7}$$

− Energy equation

$$\frac{\partial}{\partial t}\left[\rho(e + \frac{V^2}{2})\right] +$$
$$\frac{\partial}{\partial x_j}\left[\rho u_i(e + \frac{V^2}{2}) + P + q_j - u_i\tau_{ij}\right] = 0 \tag{8}$$

Where u represents the mean velocity components, ρ the density of gas, u' the fluctuating component of velocity due to turbulence, P the mean pressure, μ the molecular viscosity, V the velocity modulus, δ_{ij} Kronecker Delta, τ_{ij} the viscous shear tensor, q_j the heat flux, and e the internal energy. Additionally, the equation of state is considered if the fluid is assumed to be an ideal gas.

The Reynolds stress tensor is defined by Eq. (9):

$$-\rho\overline{u_i'u_j'} = \mu_t\left(\frac{\partial u_i}{\partial x_j} + \frac{\partial u_j}{\partial x_i}\right) - \frac{2}{3}\left(\rho k + \mu_t\frac{\partial u_k}{\partial x_k}\right)\delta_{ij} \tag{9}$$

Where k denotes the turbulent kinetic energy and μ_t the turbulent viscosity.

Reynolds stress modeling is necessary to solve Eq. (7) and account for turbulence caused by flow velocity fluctuations. The Boussinesq hypothesis is used in modeling methods to relate Reynolds stresses to the gradients of mean flow velocity. For this purpose, two RANS models were used in this study: the SST $k-\omega$ and the realizable $k-\varepsilon$. This choice is motivated by their extensive widespread application and validation in earlier research, and their balance between accuracy and computational costs. These are two-equation RANS models. This means that two transport equations, accounting for convection and diffusion of turbulent kinetic energy, are also solved alongside the conservation equations. Transport variables contain the turbulent kinetic energy k, its dissipation rate ε, and its specific dissipation rate ω. These variables represent the turbulent kinetic energy and the rate of its dissipation within the flow.

3.1.1 Realizable $k-\varepsilon$ Model

Introduced by Shih et al. (1995), this model has been validated under various flow scenarios, including separation and recirculation flows, boundary layer flows, as well as free flows such as mixing layers and jets, and rotating homogeneous shear flows (Shih et al., 1995; Nicolás-Pérez et al., 2017). The term "realizable" refers to the fact the model aligns with physical principles of turbulent flows by adhering to specific mathematical constraints related to Reynolds stresses. The model equations for the turbulence quantities k, ε, and μ_t are defined as follows (Shih et al., 1995; Mulvany et al., 2004; Hao et al., 2024):

$$\frac{\partial(\rho k)}{\partial t} + \frac{\partial(\rho k u_j)}{\partial x_j} = \frac{\partial}{\partial x_j}\left[\left(\mu + \frac{\mu_t}{\sigma_k}\right)\frac{\partial k}{\partial x_j}\right] +$$
$$G_k + G_b - \rho\varepsilon - Y_M + S_k \tag{10}$$

$$\frac{\partial(\rho\varepsilon)}{\partial t}+\frac{\partial(\rho\varepsilon u_j)}{\partial x_j}=\frac{\partial}{\partial x_j}\left[\left(\mu+\frac{\mu_t}{\sigma_\varepsilon}\right)\frac{\partial\varepsilon}{\partial x_j}\right]+$$

$$\rho C_1 S\varepsilon-\rho C_2\frac{\varepsilon^2}{k+\sqrt{\nu\varepsilon}}+C_{1\varepsilon}\frac{\varepsilon}{k}C_{3\varepsilon}G_b+S_\varepsilon \qquad (11)$$

$$\mu_t=\rho C_\mu\left(k^2/\varepsilon\right) \qquad (12)$$

Where are: $C_1=\max\left[0.43;\eta/(\eta+5)\right]$, $\eta=S(k/\varepsilon)$, $S=\sqrt{2S_{ij}S_{ij}}$, (C_2=1.9, $C_{1\varepsilon}$=1.44) model constants, (σ_k=1.0, σ_ε=1.2) the turbulent Prandtl numbers, S_{ji} the mean vorticities, (S_k, S_ε) user-defined source terms, G_k the generation of turbulence kinetic energy caused by the gradients of mean velocity, G_b the buoyancy-induced turbulence kinetic energy generation, η the mean strain rate, Y_M the contribution of fluctuating dilatation to the overall dissipation rate in compressible turbulence. As for C_μ, it depends on the turbulence fields of k and ε, as well as the mean strain and rotation rates derived from the angular velocity of the system rotation.

3.1.2 SST $k-\omega$ Model

The SST $k-\omega$ model, proposed by Menter (1994), combines the freestream independence of the standard $k-\varepsilon$ model in the far-field regions with the accurate near-wall treatment of the standard $k-\omega$ model (Qiu et al., 2024). The advantages of these two turbulence models were combined using a blending function F_1. This model outperforms most RANS models in predicting flow separation and also shows good performance under adverse pressure gradient conditions (Menter, 1994; Nicolás-Pérez et al., 2017). The model equations for the turbulence quantities k, ω, and μ_t are defined as follows (Menter, 1994; Mulvany et al., 2004; Qiu et al., 2024):

$$\frac{\partial(\rho k)}{\partial t}+\frac{\partial(\rho k u_i)}{\partial x_i}=\frac{\partial}{\partial x_j}\left(\Gamma_k\frac{\partial k}{\partial x_j}\right)+G_k-Y_k+S_k \qquad (13)$$

$$\frac{\partial(\rho\omega)}{\partial t}+\frac{\partial(\rho\omega u_j)}{\partial x_j}=\frac{\partial}{\partial x_j}\left(\Gamma_\omega\frac{\partial k}{\partial x_j}\right)+$$

$$G_\omega-Y_\omega+D_\omega+S_\omega \qquad (14)$$

$$\mu_t=\frac{\rho k}{\omega}\bigg/\max\left[\frac{1}{\alpha^*},\frac{SF_2}{a_1\omega}\right] \qquad (15)$$

Where: a_1=0.31 is a model constant, F_2 is another blending function, S represents the strain rate magnitude, (S_k, S_ω) are user-defined source terms, α^* is the damping coefficient of turbulent viscosity, (Y_k, Y_ω) denote the dissipation of k and ω because of turbulence, D_ω is the cross-diffusion term, (Γ_k, Γ_ω) are the effective diffusivities of k and ω, G_k is the generation of turbulence kinetic energy from gradients of mean velocity, and G_ω denotes the generation of specific turbulent dissipation rate.

3.2 Hypothesis and Boundary Conditions

This research adopted a steady-state approach. Despite the transient nature of projectile flight, the boundary condition variation time was believed to be longer than the fluid particle residence time in the domain,

making the transient terms in the governing equations negligible compared to the convective terms (Nicolás-Pérez et al., 2017; Dali & Jaramaz, 2019). Therefore, the computations were carried out considering the steady-state boundary conditions. The atmospheric conditions, such as Mach number, atmospheric pressure, and atmospheric temperature, were obtained according to the International Civil Aviation Organization standard (ICAO, 1993). As a result, several flight scenarios were simulated to determine the projectile drag coefficient at zero-yaw across several Mach numbers and flow regimes, ranging from subsonic to supersonic. The fluid considered in the computations was air, which was assumed to be an ideal gas with ICAO standard parameters and a viscosity coefficient based on the three-coefficient Sutherland law. The projectile was considered to fly with zero-yaw under compressible axisymmetric flow. The free-stream Reynolds number, calculated using the projectile diameter, varies from 1.2×10^6 to 2.4×10^6. The turbulent viscosity ratio and the turbulent intensity at the inflow were considered to be 10% and 2%, respectively.

Three boundary conditions were used throughout the computational domain (shown in Fig. 2): the axis boundary along the projectile longitudinal axis, the adiabatic no-slip wall boundary, and the far-field pressure boundary. These boundary conditions were based on similar flow domain configurations found in existing literature (Ibrahim & Filippone, 2007b; Dali & Jaramaz, 2019; Aziz et al., 2022). Table 1 presents the far-field parameter data for various Mach numbers, based on total parameters from ICAO (1993). The isentropic flow equations (16-19) of an ideal gas were applied to compute these data, taking into account the atmospheric parameters at the standard sea level conditions (p_0=101,325Pa and T_0=288.15K). These far-field data were used to initialize the entire computational domain. A set of Mach numbers ranging from 0.5 to 3.0 was considered to cover the available experimental data range and simulate the three typical flight regimes of artillery projectiles (subsonic, transonic, and supersonic).

$$p=p_0\bigg/\left[1+((\kappa-1)/2)M_a^2\right]^{\frac{\kappa}{\kappa-1}} \qquad (16)$$

$$T=T_0\bigg/\left[1+((\kappa-1)/2)M_a^2\right] \qquad (17)$$

$$V_\infty=M_a\cdot a=M_a\sqrt{\kappa RT} \qquad (18)$$

$$\rho=p/RT \qquad (19)$$

Where are: V_∞ free-stream velocity, R=287J/kgK air specific constant, ρ air density, a speed of sound, p static pressure, κ=1.4 specific heat ratio for air, M_a Mach number, and T static temperature.

3.3 Projectile Model for Computation

The projectile model must be perfectly defined by taking the exact dimensions to ensure a faithful representation of the real model. As depicted in Fig. 3, the 155mm M107 spin-stabilized artillery shell was chosen as the research model for calculating the airflow field and the aerodynamic drag coefficient at zero-yaw.
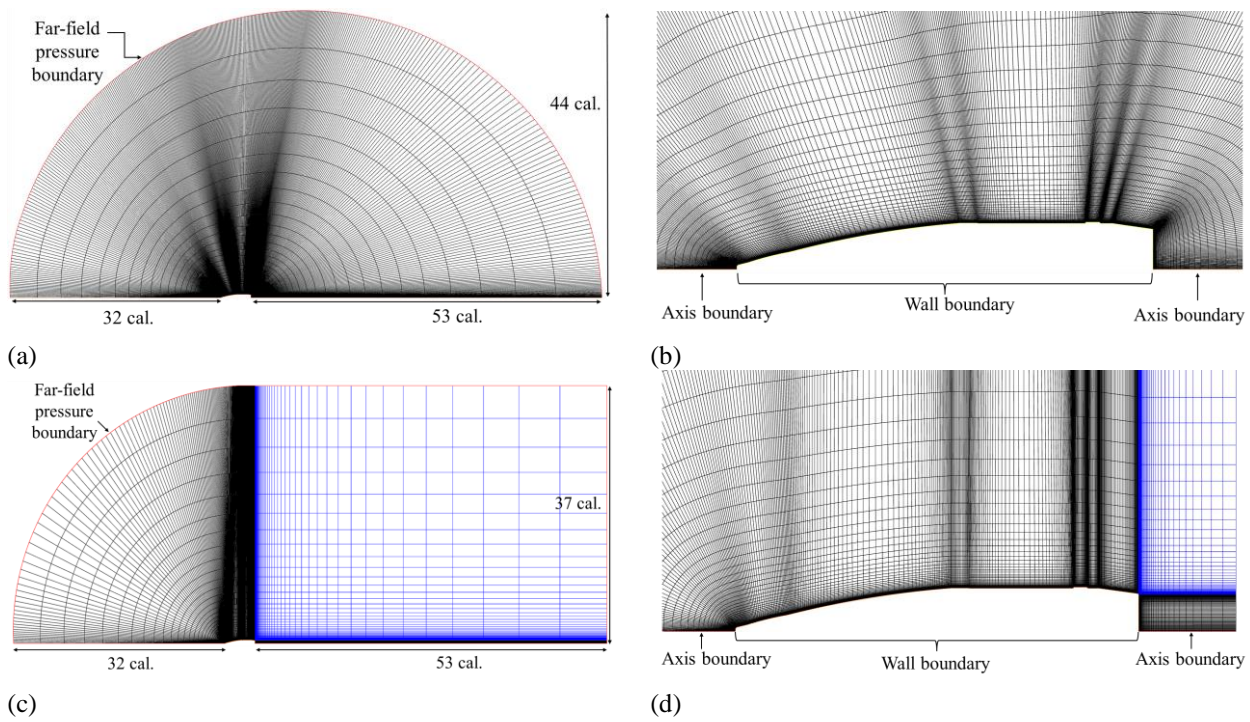
Fig. 2 Computational domain of O and C-topologies, (a, c) full domain, (b, d) mesh around the model

Table 1 Values of the far-field parameter

| Mach number M_a (/)	Pressure p (Pa)	Temperature T (K)	Velocity V_∞ (m/s)	Density ρ (kg/m³)
0.50	85,418.92	275.14	166.19	1.082
0.60	79,439.20	269.50	197.39	1.027
0.70	73,048.02	263.11	227.54	0.968
0.80	66,471.39	256.12	256.56	0.904
0.90	59,909.43	248.62	284.38	0.839
0.95	56,687.28	244.73	297.81	0.807
1.00	53,528.15	240.75	310.93	0.775
1.10	47,455.99	232.61	336.19	0.711
1.20	41,784.10	224.30	360.15	0.649
1.50	27,601.24	199.24	424.29	0.483
2.00	12,949.79	160.50	507.75	0.281
2.50	5,930.32	128.40	567.68	0.161
3.00	2,758.44	103.18	610.66	0.093
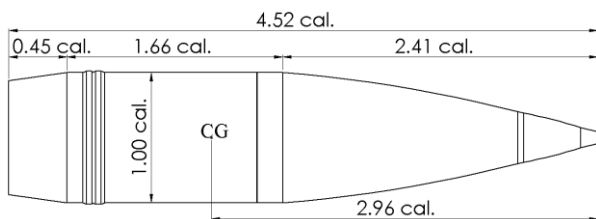
Fig. 3 Dimensions in caliber of 155mm M107 projectile model

This projectile is a rigid body with a reference diameter (cal.) of 155 mm. Its geometric dimensions are as follows: total body length 4.51 cal., nose length 2.41 cal., boattail length 0.45 cal., cylindrical body length 1.66 cal., and center of gravity (CG) from the nose 2.96 cal. These dimensional data were provided by McCoy (1998). The projectile initial velocity is often significant, reaching supersonic Mach numbers and possibly dropping below the speed of sound along its path, passing through three flow regimes.

3.4 Grid Generation

The computational domain is discretized from the projectile model (lower limit) to an upper limit defined in the far-field zone where the flow is assumed to be undisturbed. Two structured quadrilateral grids were generated by mesh generator software using the mapped meshing scheme, as shown in Fig. 2. One grid for the O-topology and the other for the C-topology. These two topologies are selected based on their common use in previous projectile aerodynamic research. Given the symmetry of the physical domain (axisymmetric projectile flying under axisymmetric flow), it is enough to generate half of the 2D domain, divided into 5 faces for the O-shaped topology and into 6 faces for the C-shaped topology. The first edge spacing was configured at 5×10^{-6}

Table 2 Computational domain characteristics

Topology type	Total number of cells	Number of cells in all directions	Number of cells on the model	Upstream extent (cal.)	Downstream extent (cal.)	Radial extent (cal.)
O-grid	39,140	95	412	32	53	44
C-grid	48,165	95	412	32	53	37

Table 3 Values of two cell quality factors examined

Topology type	EquiAngle skewness		Orthogonal quality	
	Average value	Maximum value	Average value	Minimum value
O-grid	0.14	0.57	0.92	0.24
C-grid	0.05	0.49	0.97	0.18

cal. (7.6×10^{-4} mm). This choice leads to y^+ values consistently below 0.5 across the investigated Mach number range, which is sufficient for capturing the boundary layer. Additionally, all grid stretching ratios toward the far field were maintained at 1.15 or lower. Table 2 summarizes the characteristics of the two grid topologies.

Even with 95 cells in all directions for both topologies, the C-grid contains 9,025 (95×95) more cells than the O-grid, as illustrated in Table 2 and highlighted in blue in Figs. 2(c) and (d). This is justified by the fact that the O-grid has node lines where the last node wraps around and meets the first node, hence creating an O-shape. In contrast, the first node and the last node of the same line do not meet in the C-grid case, creating a C-shaped. This distinction leads to an additional number of cells compared to the O grid case.

The grid characteristics in Table 2 were chosen after conducting a sensitivity analysis in the Mach number range considered, i.e., from 0.5 to 3.0. Six grid resolutions ($G_1, G_2, ..., G_6$) were examined for each grid topology. The coarsest G_1 consists of 9,170 cells in the O-grid case and 10,395 cells in the C-grid case, while the finest grid G_6 contains 69,120 cells in the O-grid case and 87,345 cells in the C-grid case. The first edge spacing (5×10^{-6} cal.) was not changed in all grids, whereas the number of cells next to the projectile model was altered by varying stretching ratios. The results of this grid resolution study are presented in the fourth section, "results and discussions".

3.5 Grid Quality Assessment

The grid quality is critical to obtaining exact, reliable, and, most importantly, converged results. Excessively deformed cells might result in unstable computations and erroneous findings. For a structured grid, these cells should be generated as closely as feasible to a square or rectangle. Figure 4 provides an example of a deformed quadrilateral cell. To assess the cell quality of both
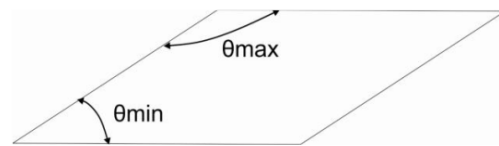

Fig. 4 Distorted 2D cell

generated grids, two quality factors were examined: EquiAngle Skewness (EAS) and Orthogonal Quality (OQ). The average values of these factors were evaluated according to the recommended quality scale shown in Fig. 5. An average EAS value close to zero indicates improved grid quality. As for the OQ factor, it is inversely proportional; a grid with better quality must have an average value close to one.

Table 3 presents the average values of EAS and OQ factors for the two grid topologies investigated, along with their respective maximum and minimum values. In both cases, the maximum EAS value is less than 0.6, and the average is below 0.15. As for the OQ factor, its minimum value is greater than 0.17, and the average exceeds 0.92. These values show that the cells within both grids meet the quality recommendations illustrated in Fig. 5, resulting in high-quality grids that do not impact the research purposes. This ensures an objective comparative study between the two grid topologies generated as well as between the two turbulence models used.

3.6 Computations Overview

The numerical approach utilized commercial CFD software that employs the finite volume method (FVM) to solve the RANS equations. The prediction of two-dimensional (2D) compressible flow was conducted for Mach numbers ranging from 0.5 to 3.0, three distinct flow regimes. The double-precision density-based solver was used in the steady-state axisymmetric flow computations.
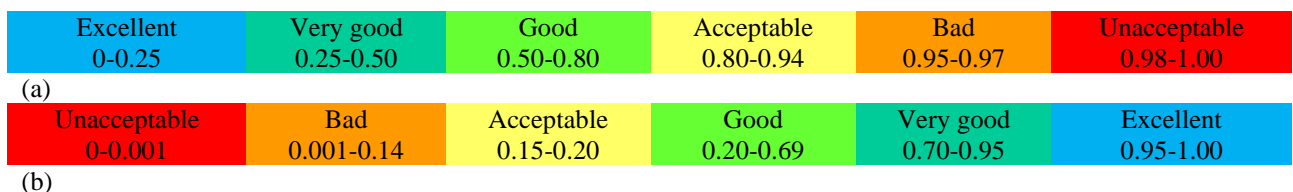

(a)

Excellent 0-0.25	Very good 0.25-0.50	Good 0.50-0.80	Acceptable 0.80-0.94	Bad 0.95-0.97	Unacceptable 0.98-1.00

(b)

Unacceptable 0-0.001	Bad 0.001-0.14	Acceptable 0.15-0.20	Good 0.20-0.69	Very good 0.70-0.95	Excellent 0.95-1.00

Fig. 5 Mesh quality spectrums, (a) EquiAngle Skewness, (b) Orthogonal Quality

Table 4 Mean value of the percent differences in C_{D0}

Topology type and turbulence model combination	G_2/G_1 (%)	G_3/G_2 (%)	G_4/G_3 (%)	G_5/G_4 (%)	G_6/G_5 (%)
O-grid & $k-\omega$	7.71	2.85	2.10	**0.82**	0.67
O-grid & $k-\varepsilon$	9.19	3.89	2.22	**0.94**	0.45
C-grid & $k-\omega$	6.96	1.19	1.19	**0.34**	0.29
C-grid & $k-\varepsilon$	5.25	1.11	**0.61**	0.21	0.23

This solver is suitable for high velocity and compressible flows and does not require stepping methods to reach convergence, unlike the pressure-based solver (Nicolás-Pérez et al., 2017). In the solver, the equation of continuity is used to compute the density field. Regarding the pressure field, it is obtained from the equation of state. Meanwhile, the momentum equation is resolved to compute the velocity field, taking into account the forces exerted on the fluid. The operating pressure was set at 0Pa. The chosen turbulence models in this study were implemented with default constant values.

The Enhanced Wall Treatment was selected for the realizable $k-\varepsilon$ turbulence model to adequately capture the flow behavior near the wall. This technique is the default for all ω-equation-based models. The reference length and area were fixed at $d=0.155m$ and $S=0.01887m^2$, respectively.

The governing equations were linearized using an implicit form with Green–Gauss node-based method for gradient term calculations and a second-order upwind scheme for spatial discretization. The convective flux terms were discretized using the Roe-FDS Scheme, proposed by Roe (1986). This scheme has proven effective for compressible flow problems (Nicolás-Pérez et al., 2017). These methods and schemes were chosen based on prior aerodynamic research (Regodić et al., 2013; Sahoo & Laha, 2014; Chang & Li, 2023). The Courant-Friedriech-Lewy (CFL) (Courant et al., 1967) number values varied from 1 to 200 depending on the changes in the solution (weakly or highly nonlinear). The number of iterations until convergence was between 700 and 2,500. This varies depending on grid topology type, turbulence model, and Mach number. The convergence is considered to be achieved once the flow residuals have diminished by at least four orders of magnitude, and the drag coefficient discrepancy was less than 0.05% over the last 100 iterations. The aerodynamic drag coefficient was the determining factor for convergence.

4. RESULTS AND DISCUSSIONS

Steady-state computations under axisymmetric flow were conducted to evaluate the performances of two grid topologies and two RANS models in estimating the zero-yaw drag C_{D0} and its components, taking the 155 mm M107 artillery projectile as the research model. This was carried out through two-dimensional (2D) computational simulations using commercial CFD software. The selected Mach numbers M_a range from 0.5 to 3.0, covering subsonic, transonic, and supersonic flight regimes. The Mach number range selection was previously discussed in subsection 3.2. Four combinations of grid topologies and

RANS turbulence models were investigated as follows: (1) O-grid with SST $k-\omega$ model, (2) O-grid with realizable $k-\varepsilon$ model, (3) C-grid with SST $k-\omega$ model, and (4) C-grid with realizable $k-\varepsilon$ model. The turbulence models were each paired with grid topologies to evaluate their combined effects in predicting the zero-yaw drag coefficient and its components. The results of this study are more reliable under steady-state and axisymmetric flow conditions without significant 3D effects or unsteady phenomena, which were not considered in the current research. In the subsections following this paragraph, both terms, "SST $k-\omega$" and "realizable $k-\varepsilon$", are replaced by "S-ko" and "R-ke", respectively, except for figures and tables.

4.1 Grid Resolution Study

As mentioned above, a grid sensitivity analysis was performed across the selected Mach number range to ensure insensitivity of the computations to the grid resolution. The study consisted of comparing the C_{D0} values as a function of M_a for six different grid resolutions, applied to each of four combinations of grid topologies and RANS turbulence models. The percent difference (P_{dif}) in C_{D0} as a function of Mach number between consecutive grid resolutions was determined according to Eq. (20). Following that, the mean percent difference over the Mach number interval of each two consecutive resolutions was calculated, as summarized in Table 4. A mean P_{dif} value of less than 1% is set as a condition to guarantee insensitivity to the grid resolution.

$$P_{dif\,(G_{i+1}/G_i)}\,(\%) = \left| \frac{C_{D0\,(G_{i+1})} - C_{D0\,(G_i)}}{(C_{D0\,(G_{i+1})} + C_{D0\,(G_i)})/2} \right| \cdot 100 \qquad (20)$$

$$i = 1, 2, ..., 5$$

Where the subscripts G_{i+1} and G_i represent two consecutive grid resolutions.

Table 4 shows that as the grid becomes finer, the mean percent difference tends to become smaller, up to values lower than 1%. The bolded values indicate the consecutive grid resolutions at which these mean values become less than 1%. Among the four combinations of grid topologies and turbulence models, three achieved a mean P_{dif} value of less than 1% starting from the fourth grid resolution, while one did so from the third resolution. It concerns the combination of the C-grid topology and the R-ke model. This combination gave results that remain insensitive with a lower number of cells compared to the other combinations. However, to ensure consistency in comparison across all combinations, the fourth resolution was chosen for further analysis.

Table 5 Absolute percent deviation (%) of C_{D0} compared to experimental data

| Flow regime	Mach number	O-grid		C-grid	
		$k-\omega$	$k-\varepsilon$	$k-\omega$	$k-\varepsilon$
Subsonic	0.50	0.50	0.51	4.36	8.89
	0.60	2.87	0.13	2.93	7.79
	0.70	4.63	0.30	1.56	6.50
Transonic	0.80	8.74	1.24	2.23	5.13
	0.90	**12.64**	3.85	6.50	1.54
	0.95	3.87	3.00	5.12	6.88
	1.00	7.94	0.07	3.87	1.56
	1.10	7.74	0.07	3.89	1.59
	1.20	7.43	0.18	3.63	1.84
Supersonic	1.50	5.79	0.70	2.57	2.42
	2.00	1.52	2.00	0.51	2.26
	2.50	1.84	3.53	2.42	3.81
	3.00	6.49	6.19	6.49	6.16
Mean value over flow regime (%)	Subsonic	2.66	0.31	2.95	7.73
	Transonic	8.06	1.40	4.21	3.09
	Supersonic	3.91	3.11	3.00	3.66
Mean value over Mach number rang (%)		5.54	1.68	3.54	4.34
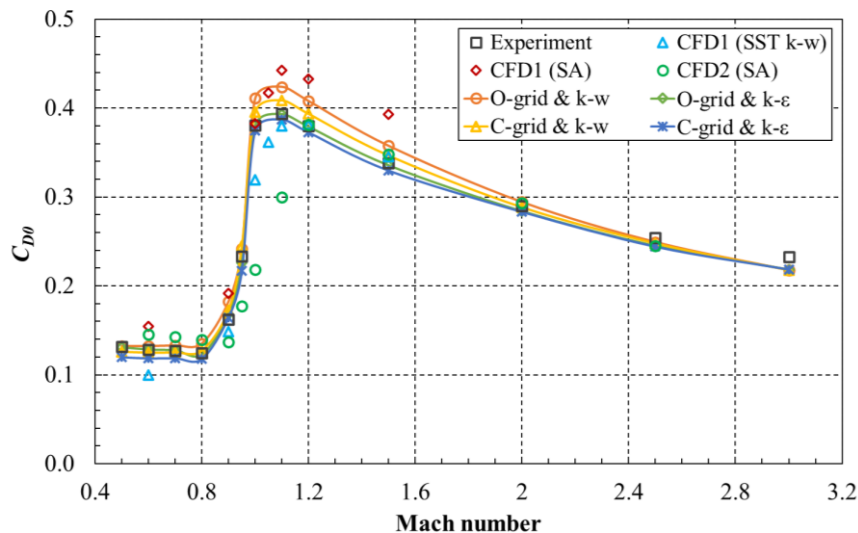
Fig. 6 Experimental and computational C_{D0} versus Mach number

4.2 Comparison of Results to Experimental and Numerical Data

The computed C_{D0} as a function of M_a was compared with the reference experimental data from McCoy (1998), as presented in Table 5 and illustrated in Figs. 6 and 7, in order to validate the computational approach. The findings were also compared to two earlier CFD studies that predicted the zero-yaw drag coefficient C_{D0} of the M107 projectile, as illustrated in Fig. 6. The first study (CFD1) by Ko et al. (2020) used two turbulence models, SST $k-\omega$ and Spalart-Allmaras (SA), over a M_a range from 0.6 to 1.5. The second study (CFD2), conducted by Wessam & Chen (2015), applied the Spalart-Allmaras (SA) turbulence model within a set of Mach numbers between 0.6 and 2.5. Both studies used a full 3D domain.

Figure 6 illustrates that the computational results obtained for the four combinations exhibit a similar trend to the experimental data. The aerodynamic drag coefficient C_{D0} remains nearly constant in the subsonic regime, followed by a distinct peak in the transonic cases, and then consistently decreases in the supersonic regime. The aerodynamic properties of the flow around the projectile explain this behavior. The flow remains steady and attached in the subsonic regime, resulting in a stable drag. When the flow changes from subsonic to supersonic in the transonic regime, a strong increase in drag is caused by shock waves that form and interact with the boundary layer. In the supersonic regime, the shock waves stabilize and become more streamlined, moving further aft along the projectile surface. This decreases the pressure drag, resulting in a progressive decrease in the overall drag coefficient. Figure 6 also illustrates that the computed results agree more closely with the reference data than those of the two earlier CFD studies in the subsonic and transonic regimes.

Table 5 shows the absolute percent deviation between the computed values and the reference data as a function
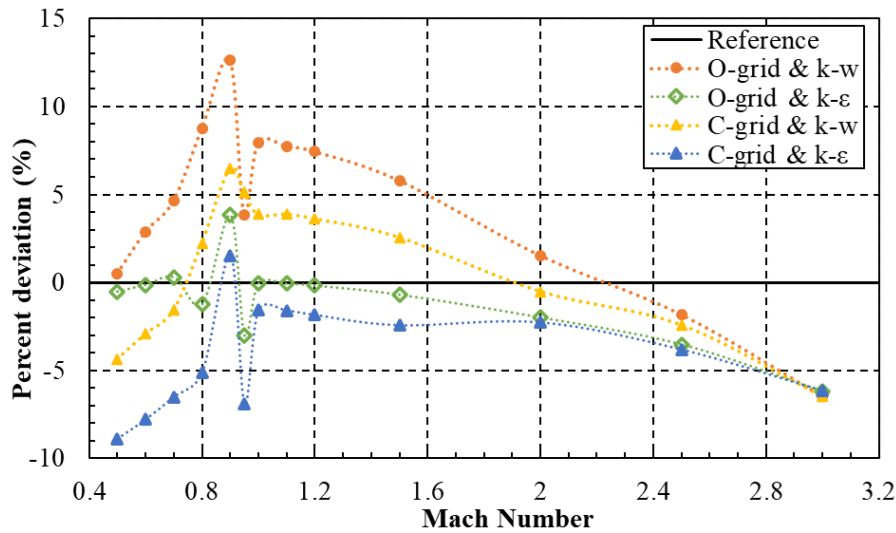
Fig. 7 Percent deviation (%) of C_{D0} versus Mach number

of both M_a and flow regime. The comparison in Table 5 and Fig. 7 was made in relative terms (percent deviation) to easily evaluate the capabilities of each combination. The percent deviation (P_{div}) between the computational (Comp) and experimental (Exp) results was calculated using Eq. (21) to quantify discrepancies and evaluate the accuracy of the selected grid topologies and turbulence models. The reference line in Fig. 7 serves as a baseline representing zero percent deviation.

$$P_{div} \ (\%) = \frac{C_{D0 \ (Comp)} - C_{D0 \ (Exp)}}{C_{D0 \ (Exp)}} \cdot 100 \qquad (21)$$

The results in Table 5 show that all predicted values from computational cases differ by less than 10% from the experimental data throughout the Mach number range, except for one value (bolded in Table 5). Furthermore, 67% of the predicted values are within a 5% deviation. The mean absolute percent deviation across all flow regimes is below 5% for all combinations, except for two cases, which show deviations of 8.06% and 7.73%. The first case pertains to the transonic regime using the combination of the O-grid topology and the S-ko model. The second case is in the subsonic regime with the combination of the C-grid topology and the R-ke model. The mean absolute percent deviation over the M_a range was also calculated, revealing varying predictive accuracy of drag coefficient C_{D0} across different combinations. The combinations are ranked by their mean absolute percent deviation from experimental data, from smallest to largest, as follows: (1) O-grid & R-ke with 1.68%, (2) C-grid & S-ko with 3.54%, (3) C-grid & R-ke with 4.34%, (4) O-grid & S-ko with 5.54%.

Figure 7 shows that in the two combinations using the R-ke model, C_{D0} results generally underpredict the reference experimental data, except for Mach 0.9. With the O-grid & R-ke combination, C_{D0} was slightly underpredicted, showing minor differences from the reference values, leading to percent deviations close to zero in the subsonic and high transonic cases. An exception was noted at Mach 3.0, with a -6.19% deviation. Regarding the C-grid & R-ke combination, C_{D0}

predictions were lower than those of the O-grid & R-ke combination for Mach number below 2.0, especially in the subsonic and early transonic regimes (Mach below 0.9), with percent deviations ranging from -8% to -5%. In the other cases, C_{D0} was slightly underpredicted, with absolute percent deviations less than 5%, except for Mach 0.95 and 3.0, which showed deviations of -6.88% and -6.16%, respectively.

The trend is completely different for the two combinations using the S-ko model, where the C_{D0} results generally overpredict the reference data across most Mach numbers, with some exceptions, as depicted in Fig. 7. In the C-grid & S-ko combination, C_{D0} was overpredicted in the transonic and low supersonic cases and underpredicted in the remaining cases, with absolute percent deviations mostly below 5%, except for Mach 0.9 and 3.0, which exhibited deviations of 6.50% and -6.49%, respectively. As for the O-grid & S-ko combination, C_{D0} predictions were higher than those in the C-grid & S-ko combination across nearly all Mach number cases. This combination showed an overprediction up to Mach 2.0, followed by an underprediction for higher Mach numbers. It exhibited significant disagreement with reference data in the transonic and low supersonic regimes, with deviation reaching up to 12.64% at Mach 0.9. For the other cases, the absolute percent deviation remained below 5%, except at Mach 3.0 with a -6.49% deviation. For the Mach 3.0 case, all combinations exhibited identical performance in predicting C_{D0}.

The obtained results align in terms of prediction accuracy with previous studies that used steady-state compressible RANS equations, and they show notably lower deviations in some cases compared to published findings. For instance, Jiajan et al. (2013) found that the predicted C_{D0} results of the 155mm M549 artillery projectile deviated by less than 5% from the free-flight aeroballistic range data across a supersonic Mach number interval, using the S-ko model with C-grid topology. Similarly, Chang & Li (2023) reported a maximum relative error of about 6% in the C_{D0} results of a 35-mm spin stabilized projectile, using the R-ke model, when

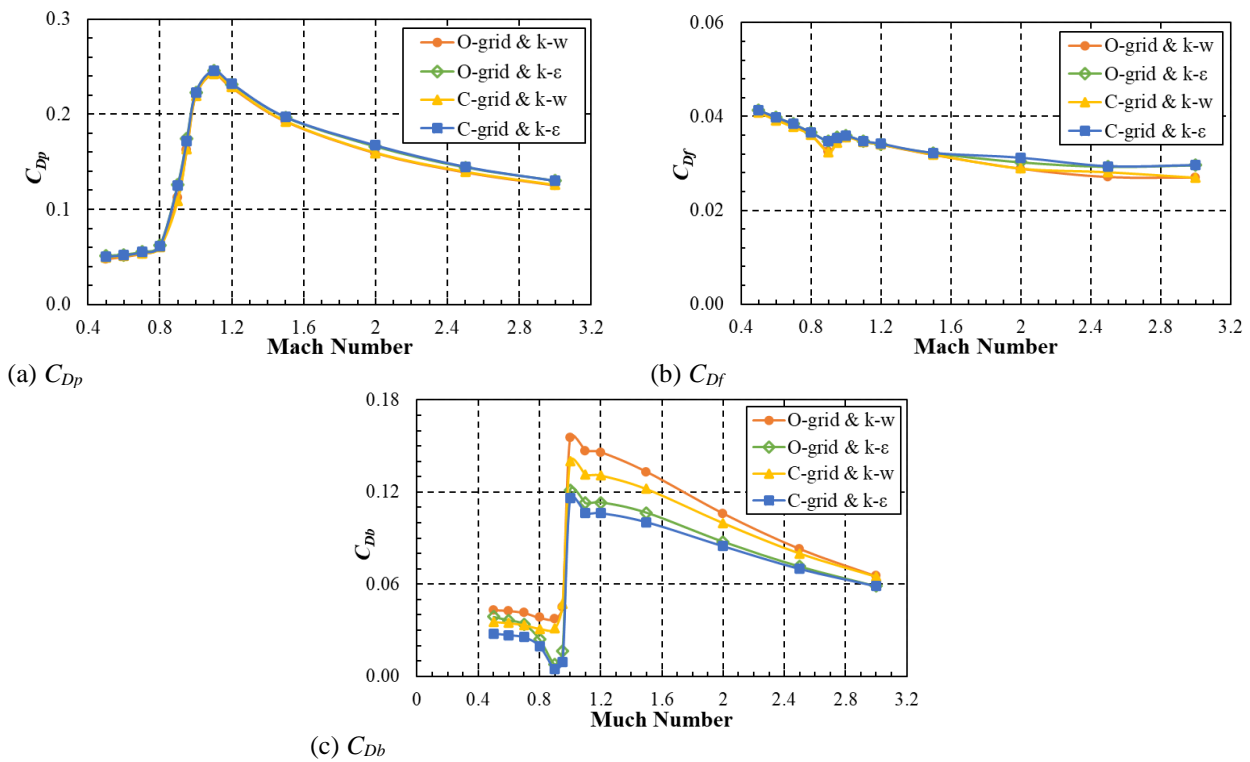(a) C_{Dp}

(b) C_{Df}

(c) C_{Db}

Fig. 8 Drag components versus Mach number

compared to wind tunnel data obtained at three supersonic speeds. In the CFD research performed by DeSpirito & Heavey (2004) using the R-ke model with O-grid topology around the projectile body, the C_{D0} of a 5-caliber projectile was founded within 10% of the experimental data over the M_a range from 0.4 to 4.5. Additionally, Nicolás-Pérez et al. (2017) reported an average absolute error in the C_{D0} numerical prediction of about 9.1% compared to experimental data of an artillery projectile across a transonic Mach number range. In contrast, the results of this research show mean percent deviation often lower than 5% over the considered M_a range and even drop below 2% when using the R-ke model with O-grid topology.

4.3 Comparison of Drag Components

To analyze discrepancies in the predicted aerodynamic drag coefficient C_{D0} across various grid topologies and turbulence model combinations, a detailed breakdown of the drag components was conducted. Figure 8 presents these components as a function of M_a for each combination. The analysis reveals that the pressure drag coefficient C_{Dp} remains nearly identical across all four combinations. Similarly, the friction drag coefficient C_{Df} shows no significant differences either. However, notable differences are obtained in the base drag coefficient C_{Db} among the combinations, leading to discrepancies in the predicted aerodynamic drag coefficient C_{D0}.

The percent differences in drag components between the different turbulence models and grid topologies were analyzed across various flow regimes, as shown in Fig. 9, in order to better understand their impact on drag component predictions. The findings illustrate that both turbulence models and grid topologies exhibit similar performance in predicting pressure drag C_{Dp} and friction

drag C_{Df} across all flow regimes, with percent differences consistently below 6% and even approaching zero in some cases. However, their predictions of the base drag component C_{Db} show considerable variability. Figure 9(a) and (b) demonstrate that the percent difference in C_{Db} between the two turbulence models ranges from 14% to 26% in the subsonic and supersonic regimes and reaches approximately 60% in the transonic regime. In contrast, the percent difference between the two grid topologies, shown in Figs. 9(c) and (d), is negligible in the supersonic regime (below 5%) but can reach up to 30% in the subsonic regime. These findings suggest that the drag component predictions are more sensitive to changes in the turbulence model than to grid topology.

Additional parameters were examined at Mach 0.9 to further investigate the discrepancies in aerodynamic drag coefficient results among the four combinations. The Mach 0.9 case represents the most unfavorable case with the highest percent difference. The examined parameters include the pressure coefficient C_P and the skin friction coefficient C_f on the projectile surface (without the base), the base pressure coefficient C_{Pb}, and Mach contours (shown in Figs. 10 and 11). It should be noted that the skin friction coefficient C_f in the projectile base is zero due to the complete detachment of the boundary layer from the base surface. As presented in Figs. 10(a) and (b), the performance consistency among the four combinations in predicting the pressure and skin friction effects on the projectile body remains evident. The C_P and C_f curves from the four combinations overlap with minimal differences in the nose and boattail regions.

The pressure coefficient C_P exhibits positive values at the nose and rotating band due to the flow stagnation in these parts. It diminishes in the cylindrical section where
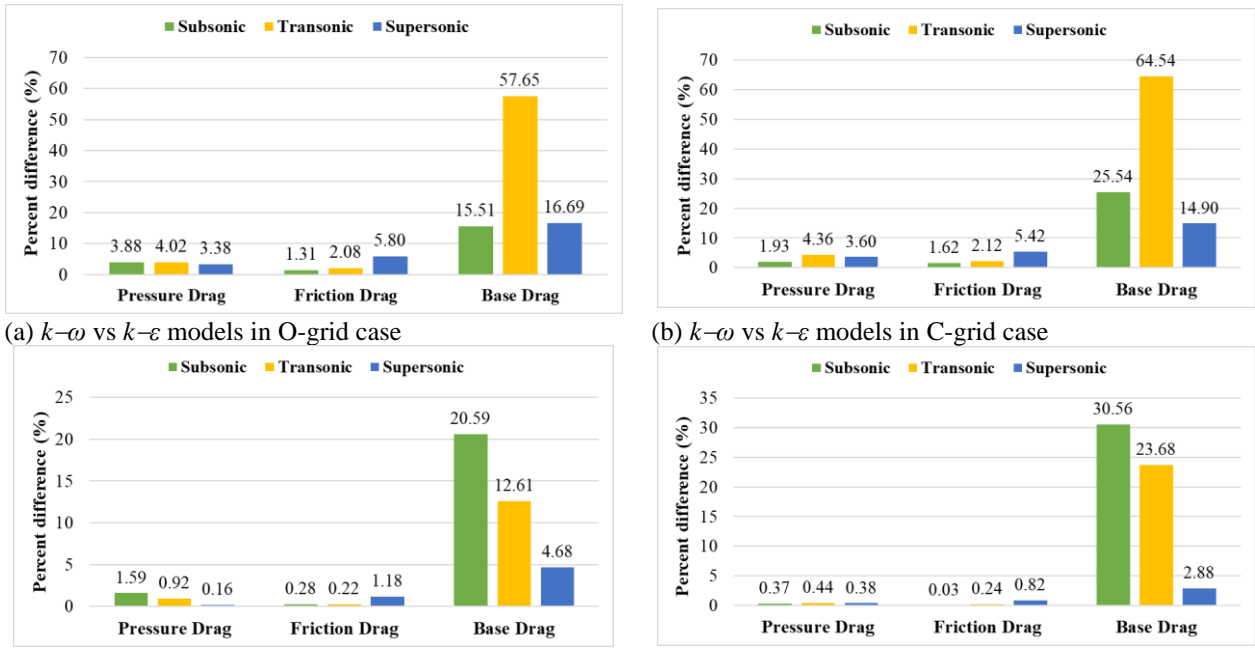
(a) $k-\omega$ vs $k-\varepsilon$ models in O-grid case

(b) $k-\omega$ vs $k-\varepsilon$ models in C-grid case

(c) O-grid vs C-grid in $k-\omega$ case

(d) O-grid vs C-grid in $k-\varepsilon$ case

Fig. 9 Percent difference of drag components versus flow regime
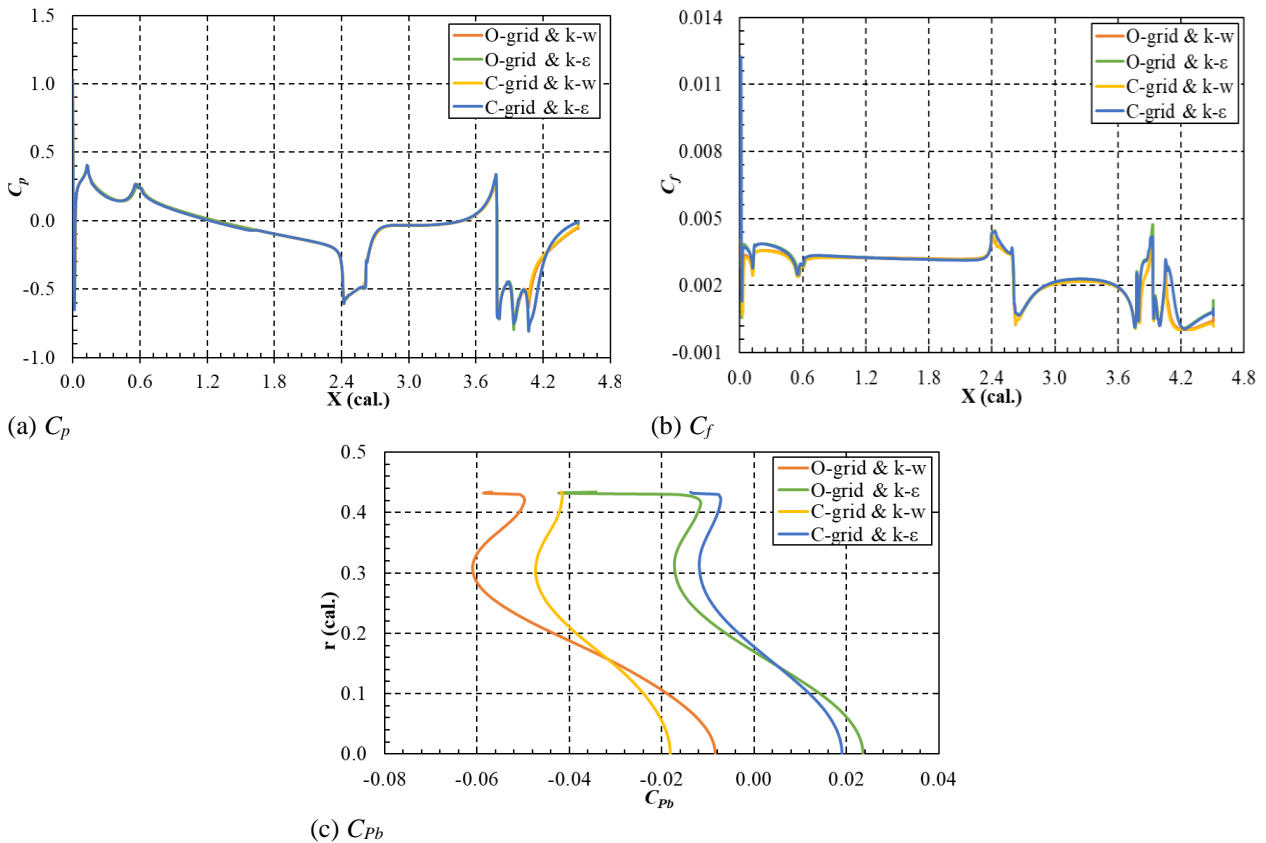

(a) C_p

(b) C_f

(c) C_{Pb}

Fig. 10 Pressure coefficient and the skin friction coefficient at M=0.90

there is no pressure gradient. In the remaining parts, i.e., at the ogive-body and the boattail-body interfaces, C_P indicates pressure drops associated with shock wave/boundary layer interaction (SBLI) at this Mach number, as shown in Fig. 11. The skin friction coefficient C_f remains relatively stable with sudden fluctuations at the ogive-body and boattail-body interfaces due to the SBLI process.

The results presented in Fig. 10(c) further highlight the significant discrepancies in predicting the fluid flow effects in the base region, especially between the turbulence models. The S-ke model predicts a stronger depression behind the projectile compared to the R-ke model. For combinations using the same grid topology, the
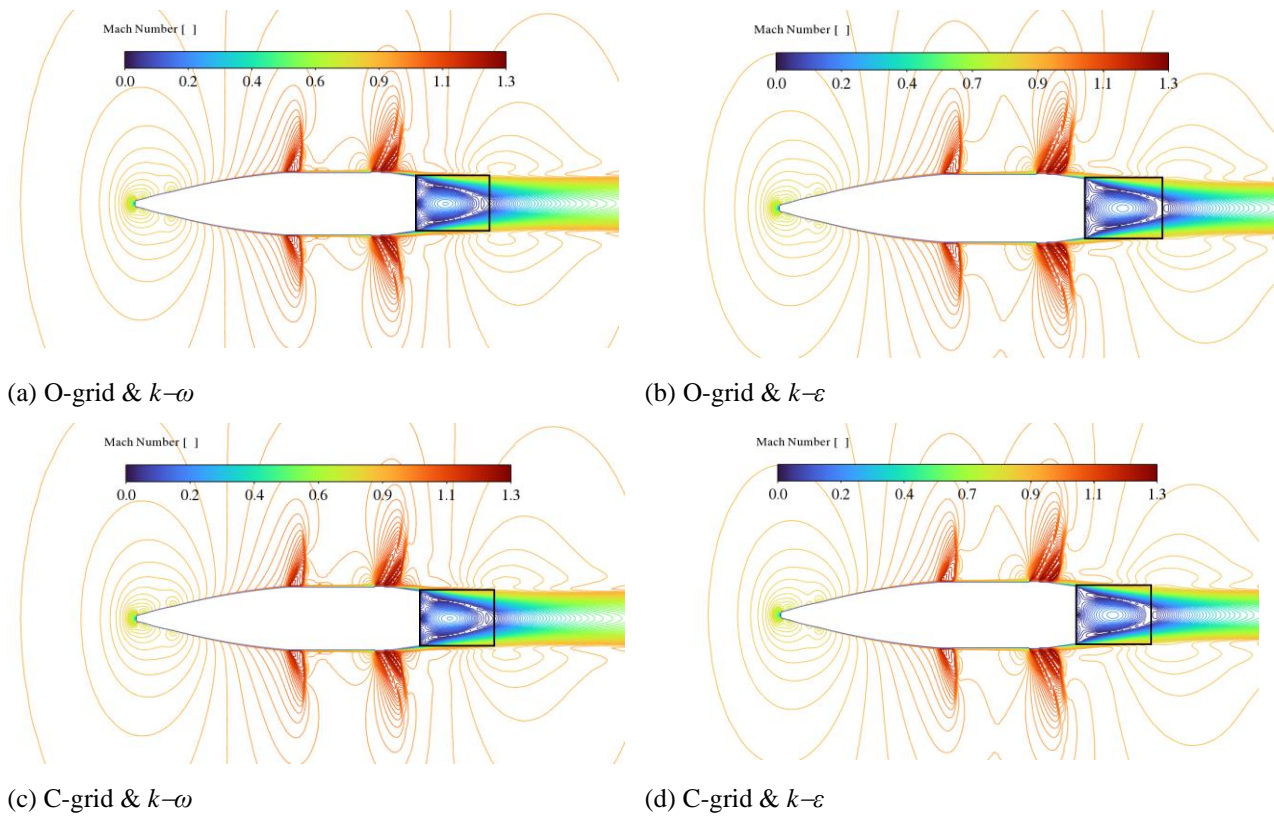
(a) O-grid & $k-\omega$

(b) O-grid & $k-\varepsilon$

(c) C-grid & $k-\omega$

(d) C-grid & $k-\varepsilon$

Fig. 11 Mach contours around the projectile at M=0.90

base pressure predictions show similar trends, especially with the R-ke model. In terms of the numerical flow field visualization around the projectile, all combinations display the same flow features, as illustrated in Fig. 11. Notably, the large deviation angle at the projectile base creates a backflow region, known as the recirculation bubble (highlighted in Fig. 11), leading to low pressure in that region. This generates base drag as a consequence of the pressure difference between the nose and base of the projectile.

5. CONCLUSION

The performance of two grid topologies (O-grid and C-grid) and two RANS turbulence models (SST $k-\omega$ and realizable $k-\varepsilon$) in predicting the aerodynamic drag coefficient of the 155 mm M107 artillery projectile at zero-yaw was investigated in this research. Four combinations of grid topology and turbulence model were examined through steady-state computational simulations across 13 Mach numbers, ranging from 0.5 to 3.0.

Two high-quality grids were generated for this research, with average EquiAngle Skewness factors of 0.14 for the O-grid and 0.05 for the C-grid. The average Orthogonal Quality factors were 0.92 for the O-grid and 0.97 for the C-grid. In the grid resolution study, the combinations performed similarly, except for the C-grid topology with the realizable $k-\varepsilon$ model, which demonstrated lower sensitivity to grid resolution compared to the other combinations.

The aerodynamic drag coefficient results from the four combinations showed good agreement with the reference data, but with varying levels of discrepancy. The combinations are ranked from the smallest to the largest mean value of absolute percent deviations over the Mach number range as follows: (1) O-grid & $k-\varepsilon$ with 1.68%, (2) C-grid & $k-\omega$ with 3.54%, (3) C-grid & $k-\varepsilon$ with 4.34%, and (4) O-grid & $k-\omega$ with 5.54%. This means that among the four studied combinations, the O-grid topology with the realizable $k-\varepsilon$ turbulence model was the most optimized combination for predicting the zero-yaw drag coefficient of the 155 mm M107 artillery projectile. The lowest mean value of absolute percent deviations (1.68%) from experimental data over the examined Mach number range justifies this selection. These deviation values of all combinations were found to be consistent with previous studies using steady-state compressible RANS equations and exhibited lower deviation levels in some cases.

The percent deviation analysis also showed that in the two combinations using the realizable $k-\varepsilon$ model, the aerodynamic drag coefficient results tend to underpredict the experimental data. Conversely, in the two combinations using the SST $k-\omega$ model, an overprediction is generally obtained, with some exceptions.

The drag component study highlighted that turbulence models and grid topologies perform equally in predicting pressure drag and friction drag across all flow regimes, with percent differences consistently below 6% and nearly zero in some cases. Also, the study revealed that base drag is the main factor behind the discrepancies in aerodynamic drag coefficient predictions, particularly in the transonic regime, where percent differences in base drag between the two turbulence models reached around 60% in both O- and C-grid cases.

Moreover, the research indicates that drag component predictions are more sensitive to changes in the turbulence model than to changes in grid topology. The base pressure coefficient of the most unfavorable case, which exhibited the highest percent difference, revealed that the SST $k-\omega$ model predicts a more pronounced low-pressure region behind the projectile compared to the realizable $k-\varepsilon$ model. The steady state flow assumption in this study may partially explain these discrepancies in base drag results between the two turbulence models. As a bluff body, a projectile often experiences vortex shedding in its wake, a process that may not be fully captured under steady-state conditions.

For future prospects, this research can be extended to three-dimensional flow simulations to further evaluate grid topologies and RANS turbulence models in predicting static and dynamic aerodynamic coefficients.

ACKNOWLEDGEMENTS

CONFLICT OF INTEREST

The authors declare that they have no conflict of interest.

AUTHORS CONTRIBUTION

A. Ferfouri: Conceptualization, Investigation, Writing original draft, Methodology, Software, Visualization. **D. D. Jerković:** Conceptualization, Project administration, Supervision, Writing – review & editing, Validation. **N. Hristov:** Resources, Writing – review & editing, Validation. **A. V. Kari:** Writing – review & editing. **T. Allouche:** Investigation, Resources.

REFERENCES

Abou-Elela, H., Ibrahim, A., Mahmoud, O., & Abdel-Hamid, O. (2013, 28-30 May). *Ballistic Analysis of a Projectile Provided with Base Bleed Unit.* 15th International Conference on Aerospace Science and Aviation Technology. Cairo, Egypt. https://doi.org/10.21608/asat.2013.22270

Aziz, M., Ibrahim, A., Riad, A., & Ahmed, Y. (2022). Live firing and 3D numerical investigation of base bleed exit configuration impact on projectile drag. *Advances in Military Technology, 17*(1), 137-152. https://doi.org/10.3849/aimt.01529

Belaidouni, H., Živković, S., & Samardžić, M. (2016). Numerical simulations in obtaining drag reduction for projectile with base bleed. *Scientific Technical Review, 66*(2), 36-42. https://doi.org/10.5937/STR1602036B

Carlucci, D., & Jacobson, S. (2008). *Ballistics: theory and design of guns and ammunition.* 496p. Florida, United States. CRC Press. ISBN: 978-1-4200-6618-0

Chang, S., & Li, D. (2023). Aerodynamic coefficients of a microspoiler for spin-stabilized projectiles. *Journal of Spacecraft and Rockets, 60*(3). https://doi.org/10.2514/1.A35566

Courant, R., Friedrichs, K., & Lewy, H. (1967). On the partial difference equations of mathematical physics. *IBM Journal of Research and Development, 11*(2), 215–234. https://doi.org/10.1147/rd.112.0215

Dali, M., & Jaramaz, S. (2019). Optimization of artillery projectiles base drag reduction using hot base flow. *Thermal Science, 23*(1), 353-364. https://doi.org/10.2298/TSCI180413210D

Decrocq, C., Martinez, B., Albisser, M., Dobre, S., Gnemmi, P., Bailly, Y., & Roy, J. (2018). Aerodynamic prediction of a projectile fitted with fins. *International Journal of Numerical Methods for Heat and Fluid Flow, 28*(5), 1218-1236. https://doi.org/10.1108/HFF-06-2017-0259

DeSpirito, J. (2008, 18 - 21 August). *Effects of base shape on spin-stabilized projectile aerodynamics.* 26th AIAA Applied Aerodynamics Conference. Hawaii, USA. https://doi.org/10.2514/6.2008-6738

DeSpirito, J. (2017, 5-9 June). *CFD aerodynamic characterization of 155-mm projectile at high angles-of-attack.* 35th AIAA Applied Aerodynamics Conference. Colorado, USA. https://doi.org/10.2514/6.2017-3397

DeSpirito, J., & Heavey, K. (2004, 16-19 August). *CFD Computation of Magnus Moment and Roll Damping Moment of a Spinning Projectile.* AIAA Atmospheric Flight Mechanics Conference and Exhibit. Rhode Island, USA. https://doi.org/10.2514/6.2004-4713

Elawwad, E., Ibrahim, A., Elshabkaa, A., & Riad, A. (2020). Flow computations past a triangular boattailed projectile. *Defence Technology, 16(3)*, 712-719. https://doi.org/10.1016/j.dt.2019.08.009

Ferfouri, A., Allouche, T., Jerković, D., Hristov, N., Vučković, M., & Benmeddah, A. (2023). Prediction of drag aerodynamic coefficient of the 155mm projectile under axisymmetric flow using different approaches. *Journal of the Serbian Society for Computational Mechanics, 17(2)*, 69-86. https://doi.org/10.24874/jsscm.2023.17.02.06

Guilmineau, E., Visonneau, M., & Rubino, G. (2020, 25-28 February). *Evaluation of turbulence models for the prediction of vortex interaction over a fighter aircraft.* Aerospace Europe Conference. Bordeaux, France. https://hal.science/hal-03027410v1

Hao, B., Jiang, Q., Xu, C., & Liu, L. (2024). Aerodynamic characterization of bullet heads with different arcuate curves . *Journal of Applied Fluid Mechanics, 17(5)*, 1015-1026. https://doi.org/10.47176/jafm.17.05.2333

Ibrahim, A., & Filippone, A. (2007a). Effect of streamwise slots on the drag of a transonic projectile. *Journal of Aircraft, 44*(6), 1865-1875. https://doi.org/10.2514/1.30439

Ibrahim, A., & Filippone, A. (2007b). Effect of porosity strength on drag reduction of a transonic projectile. *Journal of Aircraft, 44*(1), 310-316. https://doi.org/10.2514/1.23613

ICAO. (1993). Manual of the ICAO standard atmosphere extended to 80 kilometres (262 500 feet). *International Civil Aviation Organization, Doc 7488/3*

Jiajan, W., Chue, R. S., Nguyen, T., & Yu, S. (2013). Optimisation of round bodies for aerodynamic performance and stability at supersonic speeds. *Aeronautical Journal, 177*(1193), 661-685. https://doi.org/10.1017/S0001924000008368

Jiajan, W., Chue, R., Nguyen, T., & Yu, S. (2015a). Boattail juncture shaping for spin-stabilized rounds in supersonic flight. *Shock Waves, 25*(2), 189-204. https://doi.org/10.1007/s00193-015-0550-y

Jiajan, W., Chue, R., Nguyen, T., Pey, Y., & Yu, S. (2015b). Aerodynamic characteristics of high performance rounds at Mach 1.8 to 4. *Aerospace Science and Technology, 40*, 62-74. https://doi.org/10.1016/j.ast.2014.10.013

Ko, A., Chang, K., Sheen, D., Lee, C., Park, Y., & Park, S. (2020). Prediction and analysis of the aerodynamic characteristics of a spinning projectile based on computational fluid dynamics. *International Journal of Aerospace Engineering*. https://doi.org/10.1155/2020/6043721

Li, T., Qin, D., & Zhang, J. (2019). Effect of RANS Turbulence model on aerodynamic behavior of trains in crosswind. *Chinese Journal of Mechanical Engineering, 32*(1). https://doi.org/10.1186/s10033-019-0402-2

Lutton, M. J. (1989). *Comparison of C-and O-grid generation methods using a NACA 0012 airfoil* [Doctoral dissertation, Air Force Institute of Technology].

Ma, J., Chen, Z., Xue, D., Sun, X., & Liu, R. (2021). Flow separation control for a supersonic spinning projectile by using a microvortex generator jet. *Journal of Applied Mechanics and Technical Physics, 62*(2), 266-272. https://doi.org/10.1134/S0021894421020103

Ma, J., Chen, Z.-h., Huang, Z.-g., Gao, J.-g., & Zhao, Q. (2016). Investigation on the flow control of micro-vanes on a supersonic spinning projectile. *Defence Technology, 12(3)*, 227-233. https://doi.org/10.1016/j.dt.2016.01.008

McCoy, R. L. (1998). *Modern exterior ballistics.* 328p. Schiffir Publishing Ltd, ISBN: 978-0-7643-3825-0

Menter, F. (1994). Two-Equation Eddy-Viscosity Turbulence Models for engineering applications. *AIAA Journal, 32*(8), 1598–1650. https://doi.org/10.2514/3.12149

Mulvany, N., Chen, L., Tu, J., & Anderson, B. (2004). *Steady-state evaluation of 'two-equation' RANS (Reynolds-averaged Navier-Stokes) turbulence models for high-Reynolds number hydrodynamic flow simulations.* DSTO Platform Sciences Laboratory, DSTO-TR-1564. https://apps.dtic.mil/sti/tr/pdf/ADA426359.pdf

Nicolás-Pérez, F., Velasco, F., García-Cascales, J., Otón-Martínez, R., López-Belchí, A., Moratilla, D., Rey, F., Laso, A. (2017). On the accuracy of RANS, DES and LES turbulence models for predicting drag reduction with base bleed technology. *Aerospace Science and Technology, 67*, 126-140. https://doi.org/10.1016/j.ast.2017.03.031

Onn, S., Su, A., Wei, C., & Sun, C. (2001). Computational drag and magnus force reduction for a transonic spinning projectile using passive porosity. *Computer Methods in Applied Mechanics and Engineering, 190(46-47)*, 6125-6139. https://doi.org/10.1016/S0045-7825(01)00210-9

Paul, S., Vinoth Raj, A., & Senthil Kumar, C. (2023). Inward turning base-bleed technique for base drag reduction. *The Aeronautical Journal, 127*, 370–397. https://doi.org/10.1017/aer.2022.65

Qiu, N., Li, M., Wu, J., Zhu, H., & Xu , P. (2024). Numerical investigation of vortex generator on controlling flow field of centrifugal pump based on response surface method. *Journal of Applied Fluid Mechanics, 17(8)*, 1774-1791. https://doi.org/10.47176/jafm.17.8.2293

Qu, S., Liu, S., & Ong, M. (2021). An evaluation of different RANS turbulence models for simulating breaking waves past a vertical cylinder. *Ocean Engineering, 234*(5). https://doi.org/10.1016/j.oceaneng.2021.109195

Regodić, D., Jevremovic, A., & Jerković, D. (2013). The prediction of axial aerodynamic coefficient reduction using base bleed. *Aerospace Science and Technology, 31*(1), 24-29. https://doi.org/10.1016/j.ast.2013.09.001

Roe, P. (1986). Characteristic-Based Schemes for the Euler Equations. *Annual Review of Fluid Mechanics, 18*(1), 337–365. https://doi.org/10.1146/annurev.fl.18.010186.002005

Roy, A. (2012). *A first course on aerodynamics.* 95p. Ventus Publishing ApS, ISBN: 978-87-7681-926-2.

Sahoo, S., & Laha, M. (2014). Coefficient of drag and trajectory simulation of 130 mm supersonic artillery shell with recovery plug or fuze. *Defence Science Journal, 64*(6), 502–508. https://doi.org/10.14429/dsj.64.8110

Shih, T. H., Liou, W., Shabbir, A., Yang, Z., & Zhu, J. (1995). A new k-ε eddy viscosity model for high reynolds number turbulent flows. *Computers & Fluids*, 24(3), 227-238. https://doi.org/10.1016/0045-7930(94)00032-T

Silton, S. (2005). Navier–Stokes computations for a spinning projectile from subsonic to supersonic speeds. *Journal of Spacecraft and Rockets, 42*(2), 223-231. https://doi.org/10.2514/1.4175

Silton, S. (2011, 27 - 30 June). *Navier-Stokes predictions of aerodynamic coefficients and dynamic derivatives of a 0.50-cal projectile.* 29th AIAA Applied Aerodynamics Conference. Hawaii, USA. https://doi.org/10.2514/6.2011-3030

Thomas, B., & Agarwal, R. (2019). Evaluation of various rans turbulence models for predicting the drag on an ahmed body. *AIAA AVIATION Forum*. Dallas, USA. https://doi.org/10.2514/6.2019-2919

Wang, M., & Zhuo, C. (2021). Numerical research on effect of base bleed type on operation process of base bleed projectile. *Journal of Applied Fluid Mechanics, 14*(5), 1583-1591. https://doi.org/10.47176/jafm.14.05.32343

Wessam, M., & Chen, Z. (2015, January). *Flow field investigations and aerodynamic characteristics of artillery projectile.* International Conference of Electrical, Automation and Mechanical Engineering. https://doi.org/10.2991/eame-15.2015.73

Wu, C., Wang, Y., & Yang, X. (2014). Evaluation of various turbulence models in predicting airflow and turbulence around a generic vehicle model. *Advanced Materials Research*, 989-994, 3468-3472. https://doi.org/10.4028/www.scientific.net/AMR.989-994.3468